Journal of Materials Science & Technology 82 (2021) 122–134

Contents lists available at ScienceDirect

Journal of Materials Science & Technology

journal homepage: www.jmst.org

Research Article

Deformation induced hcp nano-lamella and its size effect on the strengthening in a CoCrNi medium-entropy alloy

Yan Ma[a,b], Muxin Yang[a], Fuping Yuan[a,b,*], Xiaolei Wu[a,b]

[a] State Key Laboratory of Nonlinear Mechanics, Institute of Mechanics, Chinese Academy of Sciences, No. 15, West Road, North 4th Ring, Beijing, 100190, China

[b] School of Engineering Science, University of Chinese Academy of Sciences, No. 19(A) Yuquan Road, Shijingshan District, Beijing, 100049, China

ARTICLE INFO

Article history:
Received 15 October 2020
Received in revised form
17 November 2020
Accepted 1 December 2020
Available online 29 January 2021

Keywords:
Strengthening mechanisms
Phase transformation
Twinning
Medium entropy alloys
Molecular dynamics simulations

ABSTRACT

Deformation-induced hcp nano-lamellae with various widths and interspacings were observed in the CoCrNi medium-entropy alloy (MEA) under high strain rate and cryogenic temperature in the present study. Higher hardness was found in the cryogenic-deformed samples compared to the room temperature-deformed samples without hcp phase. Then, size effects of embedded hcp nano-lamellae on the tensile behaviors in the fcc CoCrNi MEA were investigated by molecular dynamics simulations. The overall strengthening was found to have two components: phase strengthening and extra interface strengthening, and the interface strengthening was observed to be always stronger than the phase strengthening. Both overall strengthening and interface strengthening were found to increase with increasing width and decreasing interspacing of embedded hcp nano-lamellae. The samples with small spaced hcp nano-lamellae are even stronger than the pure hard hcp phase due to the extra interface strengthening. The samples with larger width of embedded hcp nano-lamellae can provide stronger resistance for dislocation slip and transmission. Nanotwins were observed to be formed in the embedded hcp nano-lamellae. Higher density of phase boundaries and newly formed twin boundaries can provide more barriers for dislocation glide in the other slip systems, resulting in higher strength for samples with smaller interspacing.

1. Introduction

High-entropy alloys (HEAs) [1–3] and medium-entropy alloys (MEAs) [4–6], which consist of three or more elements typically with equal molar fraction, have attracted great interests recently due to their high strength, high ductility and exceptional fracture toughness. HEAs and MEAs are solid-solution alloys and generally are single phase materials [7,8]. Moreover, recently reported fcc CrMnCoNiFe HEA [9–12] and CoCrNi MEA [13,14] were found to have low stacking fault energy (SFE) and excellent mechanical properties, and have even better mechanical properties at cryogenic temperature than at room temperature due to a transition of the dominant deformation mechanism from dislocation activities to deformation twins (DTs) [15–18]. The observed high strength in HEAs and MEAs could be partly attributed to the lattice distortion and the solid solution strengthening. While, more recent advances have indicated that short range ordering [19–21], local chemical order [22,23], and local composition fluctuation [24], can also play important roles on the strength of HEAs and MEAs.

Previous research [8,25,26] has suggested that the SFE of the CoCrNi MEA could even be negative at 0 K, thus the CoCrNi MEA has high propensity for twinning and phase transformation at low temperatures. Previous work has also indicated that the SFE in this kind of alloys could be non-uniform and tunable locally by tailoring the local chemical short range order and the local composition fluctuation [23], which may promote twinning and phase transformation at positions with lower fluctuated SFE. Phase transformation from fcc phase to hcp phase has been widely observed in HEAs/MEAs and other alloys, such as in the CoCrNi MEA [27,28], in the $CoCrFeNiMo_{0.15}$ HEA [29], in the FeCoCrNi HEA [30], in the Co-27Cr-5Mo-0.05C alloy [31], in the CoCrWMo HEA [32], in the $Fe_{60}Co_{15}Ni_{15}Cr_{10}$ HEA [33], in the $Fe_{80-x}Mn_xCo_{10}Cr_{10}$ HEA [34], in the $FeNiCrCoAl_{0.36}$ HEA [35], and in the $Cr_{20}Mn_6Fe_{34}Co_{34}Ni_6$ HEA [36]. In these reports, the deformation modes and condi-

* Corresponding author at: State Key Laboratory of Nonlinear Mechanics, Institute of Mechanics, Chinese Academy of Sciences, No. 15, West Road, North 4th Ring, Beijing, 100190, China.

E-mail addresses: mayan@imech.ac.cn (Y. Ma), mxyang@lnm.imech.ac.cn (M. Yang), fpyuan@lnm.imech.ac.cn (F. Yuan), xlwu@imech.ac.cn (X. Wu).

https://doi.org/10.1016/j.jmst.2020.12.017
1005-0302/

tions for the deformation-induced phase transformation (from fcc to hcp) include quasi-static uniaxial tensile loading at both room and cryogenic temperatures, cold rolling at both room and cryogenic temperatures, hard turning at both room and cryogenic temperatures, dynamic shear testing at both room and cryogenic temperatures, in-situ high energy X-ray diffraction (XRD) compression tests, in-situ transmission electron microscope (TEM) tensile tests. These results [37–39] have indicated that the phase transformation can be promoted at lower temperatures, higher strain rates and larger plastic strains. Moreover, these results [27,28,30] also suggested that the formation of the thin hcp lamellae is generally achieved by the glide of Shockley partial dislocations on every other {111} planes.

The hcp lamellae with different widths and interspacings were observed to be formed under various deformation conditions in previous studies [32–34], and the phase transformation were found to play important roles on the strengthening and strain hardening in HEAs and MEAs [11,40–43] since the formed hcp phase (ε martensite) was generally thought to be stronger than the original fcc phase. Moreover, heterogeneous laminates have attracted extensive interests recently due to the fact that excellent mechanical properties can be achieved and optimized by tailoring microstructures across interfaces and interface spacing in the laminates [44–48]. Thus, in the HEAs and MEAs with transformed hcp lamellae, the lamellar structure of the hcp lamellae and the straight phase boundaries should be strong barriers for further dislocation slip, and the extra interface strengthening should be considered besides the phase strengthening.

However, how the width and interspacing of the hcp lamellae affect the mechanical properties and the corresponding deformation mechanisms is still unclear. In this regard, dynamic shear experiments have been conducted on the CoCrNi MEA at both room and cryogenic temperatures in the present study, and the hardness and the microstructures after dynamic testing under both conditions have been compared. Moreover, large-scale molecular dynamics (MD) simulations have also been performed in the present study to investigate the effects of the width and interspacing of the hcp lamellae on the strength, plastic flow behaviors and corresponding atomistic deformation mechanisms in the CoCrNi MEA. The applied strain rates were typically high (> 10^7 /s) in the MD simulations due to the inherent computation limitations [49–52], thus much higher flow stress might be induced and some deformation mechanisms (such as diffusion effects) might be limited at such short times in the simulated cells. While, MD simulations were also proven to have advantages over experiments, such as displaying the atomic transient microstructure evolution and studying the in-situ plastic deformation mechanisms (dislocation activities, grain boundary (GB) activities, twinning and phase transformation) at the atomic scale in nanostructured metals with carefully designed model systems [18,53,54]. For example, MD simulations have been indicated to be effective in investigating the size effects on the flow stress and the deformation mechanisms in nanocrystalline metals and nanotwinned metals in previous research [55,56].

2. Materials, experimental procedures and simulation techniques

The CoCrNi MEA ingots were produced via electromagnetic levitation melting in a high-purity argon atmosphere. The actual chemical composition of the ingots was determined to be 35.34Ni–30.77Cr–33.81Co (in weight%) or 34.06Ni-33.48Cr-32.46Co (in molar%), with small amount of other impurities. The ingots were homogenized at 1473 K for 12 h first, and then hot-forged into slabs with the thickness of 10 mm, at starting temperature of 1323 K. The slabs were then cold rolled (CR) into 2.7 mm thick sheets. The CR sheets were subsequently annealed at 1073 K for 1 h and immediately water quenched.

The hat-shaped plate specimens have been machined from the sheets with the impact direction perpendicular to the rolling direction. The set-up for Hopkinson-bar experiments with hat-shaped plate specimens can be referred to our previous paper [28,47]. Dynamic shear tests have been conducted under both cryogenic and room temperatures. Cryogenic temperature experiments (77 K) were conducted by immerging the specimen into a packing foam container with liquid nitrogen for 10 min before dynamic shear tests. The impact velocities of the striker bar for the dynamic shear experiments were set to be about 25 m/s and the nominal shear strain rates were estimated to be as high as 8×10^4 /s. The microstructures after dynamic shear testing have been characterized by transmission electron microscope (TEM, JEOL JEM-2100 F) and high resolution electron microscope (HREM). Thin foils were cut for TEM observations, and then mechanically ground to about 50 μm thick and finally thinned by a twin-jet polishing facility using a solution of 5 % perchloric acid and 95 % ethanol at −25 °C [28,47]. The micro-hardness measurements on the shear zone prior to and after testing were conducted on the well-polished specimens by a Vickers diamond indenter (Future-Tech FM800) under a load of 5 g for 15 s dwell time.

Large-scale Atomic/Molecular Massively Parallel Simulator (LAMMPS) code has been utilized to perform the MD simulations in the CoCrNi MEA. The EAM potential developed by Farkas [57] was applied to simulate the force reactions between atoms for the CoCrNi MEA. In this study, the 3D nanocrystalline fcc samples with embedded hcp nano-lamellae have been created using Voronoi method, and 27 grains were created and the average grain size was set to be 20 nm. For comparison, the 3D nanocrystalline pure fcc sample and pure hcp sample have also been created and investigated in the similar way. In order to visualize the defects, the atoms were colored based on common neighbor analysis (CNA), in which white color is for fcc atoms, red color is for hcp atoms and green color is for GB, dislocation cores and other disordered atoms. A single line of hcp atoms represents a twin boundary (TB), two hcp lines with a fcc line in between stand for an extrinsic SF, two adjacent hcp lines stand for an intrinsic SF (the thinnest hcp lamella), three or more adjacent hcp lines represent hcp lamella. The same CNA color rule was used in all figures. The relaxed 3D nanocrystalline pure fcc sample and pure hcp sample are displayed in Fig. 1(a) and (b). For fixed interspacing (7.34 nm), three widths of the hcp lamellae (2 hcp atom layers, 6 hcp atom layers and 10 hcp atom layers) have been considered. The typical relaxed 3D nanocrystalline fcc samples with the same interspacing (7.34 nm) while with different widths of hcp nano-lamellae (2 hcp atom layers and 10 hcp atom layers) are shown in Fig. 1(c) and (d). For fixed width of the hcp lamellae (6 hcp atom layers), six different interspacings (1.84, 2.45, 3.06, 3.67, 5.50, 7.34 nm) have been considered. The typical relaxed 3D nanocrystalline fcc samples with the same width of the hcp lamellae (6 hcp atom layers) while with different interspacings (1.84 and 5.50 nm) are shown in Fig. 1(e) and (f). The dimensions of the 3D nanocrystalline samples are $60 \times 60 \times 60$ nm^3, containing approximately 19600000 atoms. In the 3D nanocrystalline samples, the Co, Cr and Ni atoms are randomly distributed. The same Voronoi grain structure and the same crystallographic orientation for each grain are retained as the width and interspacing of the hcp lamellae change.

Periodic boundary conditions were imposed for all three directions. Before tensile testing, the as-created cells were first subjected to energy minimization by the conjugate gradient method, and then was gradually heated up to 77 K in a step-wise fashion, and then relaxed using the Nose/Hoover isobaric-isothermal ensemble (NPT) under both the pressure 0 bar in all directions and the temperature

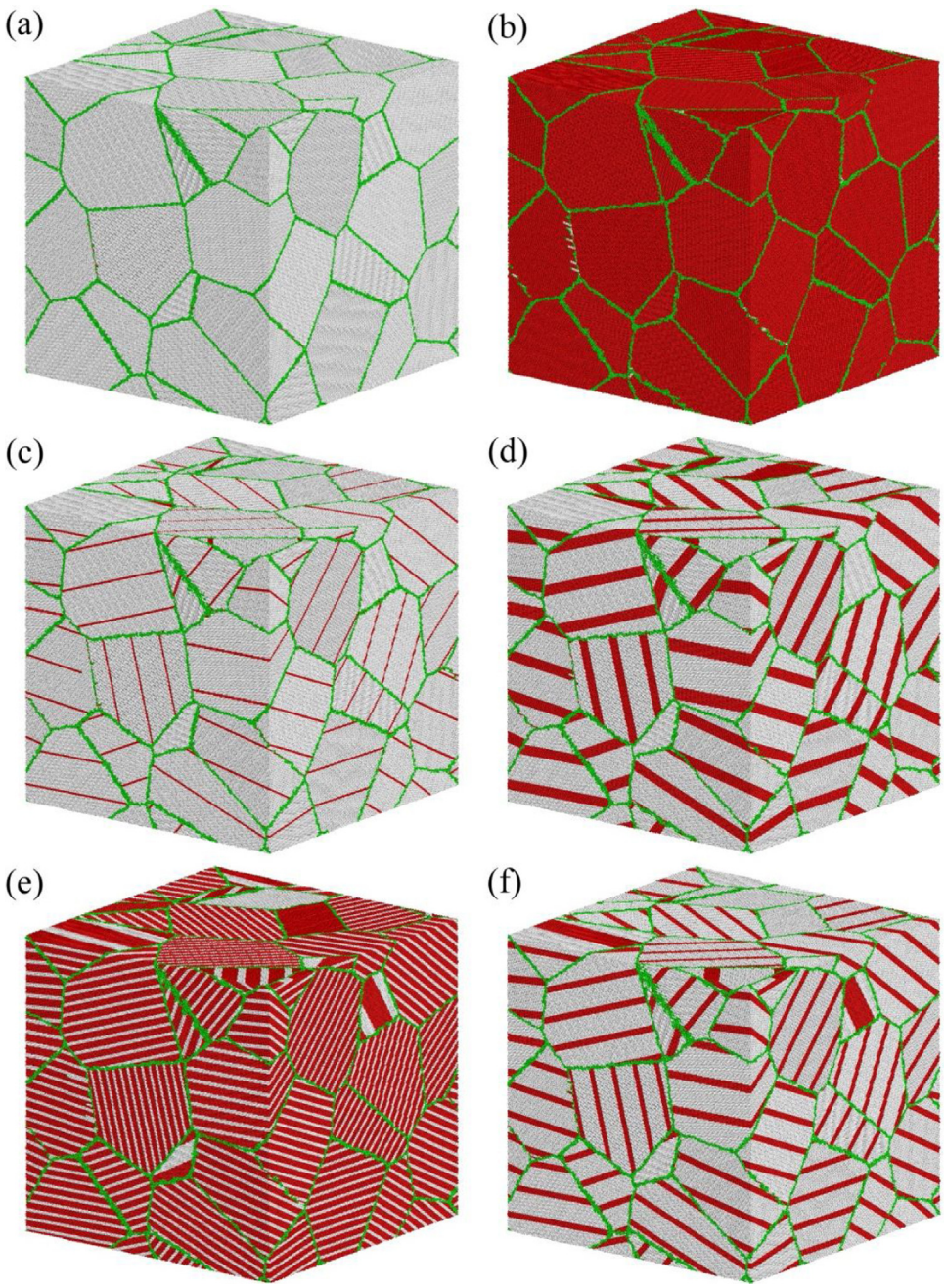

Fig. 1. The relaxed 3D simulation cells for the nanocrystalline samples (a) with pure fcc structure; (b) with pure hcp structure. (c)-(f) The relaxed 3D simulation cells for the nanocrystalline fcc samples with numerous embedded hcp nano-lamellae.

77 K for enough time to achieve equilibrium configuration. After relaxation, the tensile loading was applied along *x* direction to a strain of 10 % for each sample at a constant strain rate of 5×10^8 /s. During the tensile loading, the temperature was kept to be constant (77 K), and the pressures along the *y* and *z* directions were kept to be zero for simulating the uniaxial stress loading.

3. Results and discussions

3.1. Deformation-induced hcp nano-lamella in dynamic shear tests and its effect on the strengthening

The dynamic shear deformation under high strain rate (8×10^4 /s) has been applied to the CoCrNi MEA, and the uniform shear strain before the onset of adiabatic shear band can be as high as ~ 6 [28]. The strong strain hardening and the exceptional ductility upon impact loading under cryogenic temperature in the CoCrNi MEA can be attributed to the formations of DTs, SFs, Lomer-Cottrell locks and hcp nano-lamellae [28]. The deformation-induced hcp nano-lamellae with various widths and interspacings are shown in Fig. 2 for the CoCrNi MEA tested under cryogenic temperature and high strain rate. It is well known that the dominant deformation mechanism can be switched between DTs and phase transformation, or a mixture of the two mechanisms by regulating the SFE and the local stress/strain levels in metals and alloys [23,58,59]. Due to the locally tunable SFE [23], a zone with mixture of DTs and hcp nano-lamellae is shown by HREM image in Fig. 2(b), and a close-up view showing the stacking sequences of the fcc phase (ABCABC. . .) and the hcp phase (ABAB. . .) is displayed in Fig. 2(c). Our previous research by MD simulations [58] has indicated that the formation of

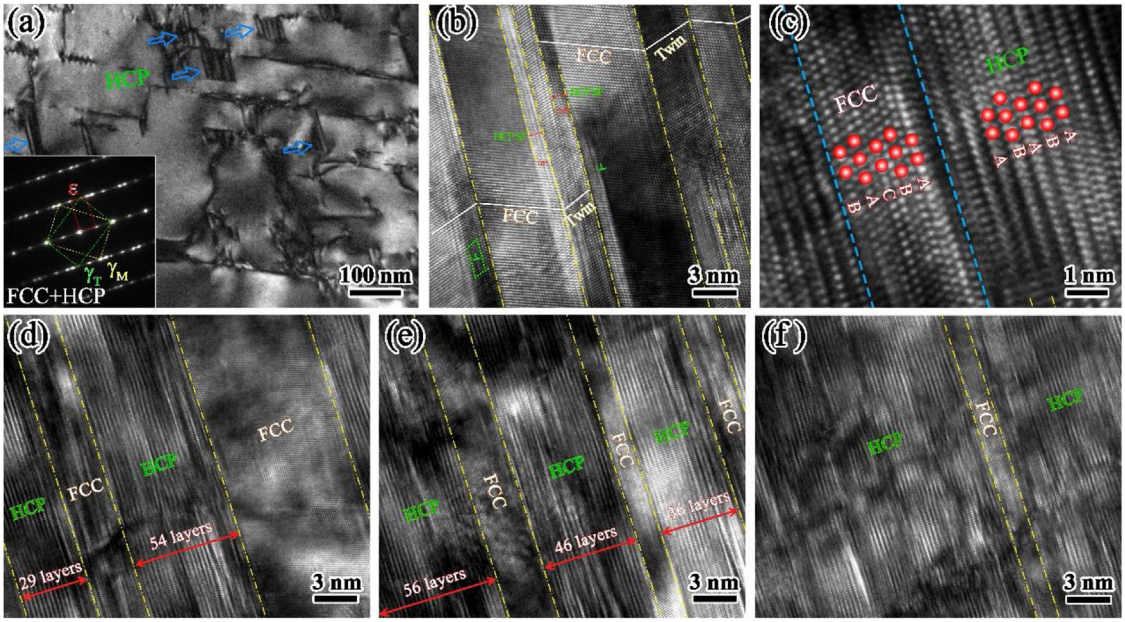

Fig. 2. Deformation-induced hcp nano-lamellae and nanotwins in the CoCrNi MEA tested under cryogenic temperature and high strain rate. (a) Bright-field TEM image showing hcp nano-lamellae; (b) HREM image showing hcp nano-lamellae and DTs; (c) HREM image showing the stacking sequences for a typical hcp nano-lamella in the fcc matrix; (d)-(f) HREM images showing the structures with hcp nano-lamellae, and the hcp phase fractions are 52 %, 71 %, 93 % in the selected areas, respectively.

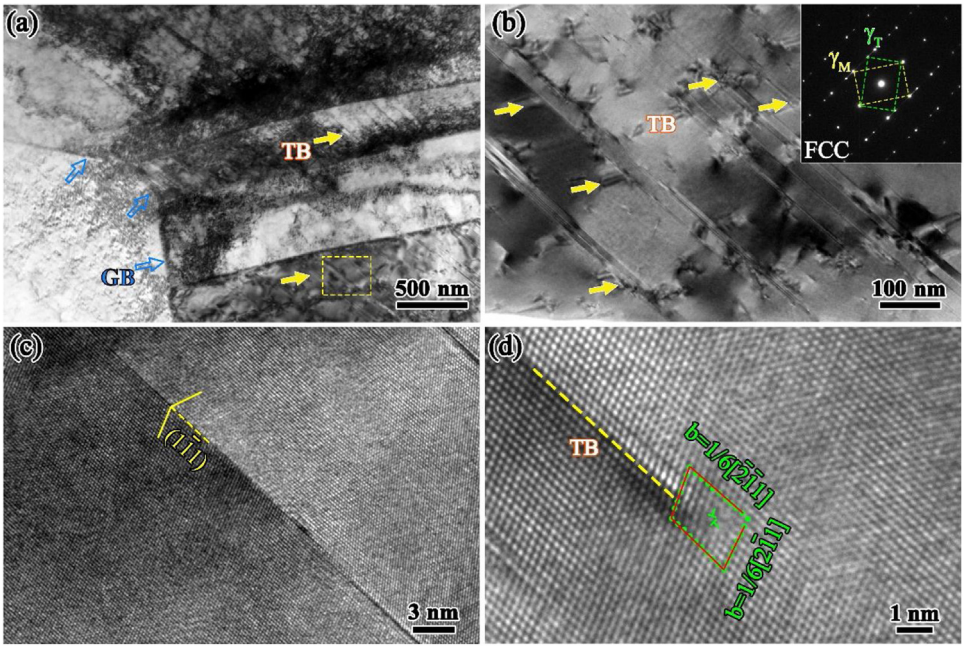

Fig. 3. Deformation-induced DTs in the CoCrNi MEA tested under room temperature and high strain rate. (a) Bright-field TEM image showing DTs; (b) Close-up views for the rectangular area in (a) showing secondary nanotwins; (c) HREM image taken with the <110> zone axis, showing orientation relationship of fcc matrix and twins; (d) HREM image showing the dislocations at the tip of TBs.

the hcp nano-lamellae can be induced by the glide of Shockley partial dislocations on every other {111} planes. In Fig. 2(d)-(f), HREM images, showing mixtures of hcp nano-lamellae and fcc matrix with different widths/interspacings of hcp nano-lamellae and different hcp phase fractions, are displayed.

In order to show the strengthening effect of the deformation-induced hcp nano-lamellae, the TEM and HREM images for the samples deformed under high strain rate (8×10^4 /s) and room temperatures are also shown in Fig. 3, and then the hardness measurements after dynamic testing under both cryogenic and room temperatures have been compared in Fig. 4. It is indicated that DTs and multiple twins have been induced under high strain rate and room temperature. Fig. 3(c) and (d) display the HREM images taken with the <110> zone axis showing the orientation relationship of fcc matrix and twins and the dislocations at the tip of TBs. These DTs and multiple twins have also observed for the samples deformed under high strain rate and cryogenic temperature. The main difference for the microstructures after dynamic shear deformation under cryogenic temperature and room temperature is that no deformation-induced hcp nano-lamella is formed after dynamic shear deformation under room temperature. These observations can be generally attributed to the lower SFE under lower

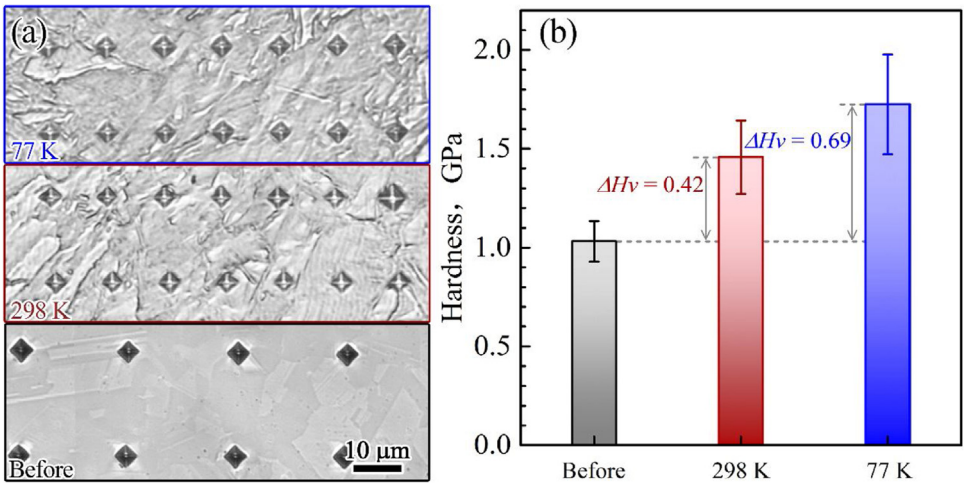

Fig. 4. Vickers microhardness of samples prior to and after dynamic deformation under both cryogenic and room temperatures. (a) Optical images of indentation arrays. (b) Vickers hardness comparison.

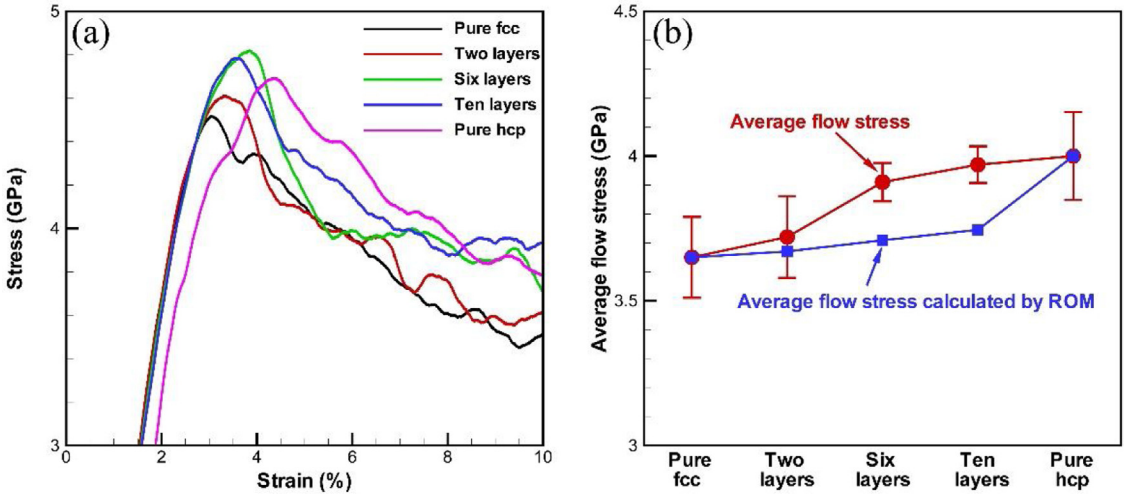

Fig. 5. (a) The simulated stress-strain curves for the nanocrystalline samples with the same interspacing (7.34 nm) and the different hcp layer widths (the curves for pure fcc and pure hcp samples are also included). (b) The effect of hcp layer width on the average flow stress.

temperature for metals and alloys. It is well known that the multiple twinning network can present more barriers for dislocation motion to contribute higher strength [17], while the formed hcp phase (ε martensite) was generally thought to be stronger than the original fcc phase [27,36], thus the higher fraction of formed hcp phase should also induce stronger strengthening. As shown in Fig. 4, the microhardness increment after dynamic shear deformation under cryogenic temperature (0.69 GPa) is much higher than that after dynamic shear deformation under room temperature (0.42 GPa). It is qualitatively evidenced that deformation-induced hcp nano-lamellae can have strong effect on the strengthening, while the effects of the width and interspacing of hcp nano-lamellae on the strengthening should be further studied. Moreover, the mechanical properties in heterogeneous laminates [48,60] can be improved by the high density of domain interfaces. Thus, extra interface strengthening should be considered in the structures with mixtures of hcp nano-lamellae and fcc matrix besides the phase strengthening, and the effects of the width and interspacing of hcp nano-lamellae on these two strengthening mechanisms should be revealed.

3.2. Effect of width of hcp nano-lamellae on the strengthening

First, the effect of the width of hcp nano-lamellae on the tensile properties is considered by MD simulations. In order to differentiate the interface strengthening from the phase strengthening, the tensile properties of the pure fcc sample and the pure hcp sample are also investigated. Fig. 5(a) shows the simulated stress-strain curves for the nanocrystalline samples with different widths of hcp nano-lamellae (the interspacing is fixed as 7.34 nm), in which the curves for pure fcc and pure hcp samples are also included. After the elastic stage, the simulated stress-strain curves start to deviate from the linear relationship for the onset of plastic deformation, and display strong strain hardening until the maxim stress point, and then the flow stresses decrease gradually to a plateau value with some fluctuations. In order to study the size effects of hcp nano-lamellae on the strengthening, it is physically more meaningful to consider the average flow stress over a certain plastic strain interval due to the overshoot phenomenon induced by the employed high strain rate in MD simulations [55,56]. Thus, the average stress over a strain interval from 6 % to 10 % is calculated for the various samples

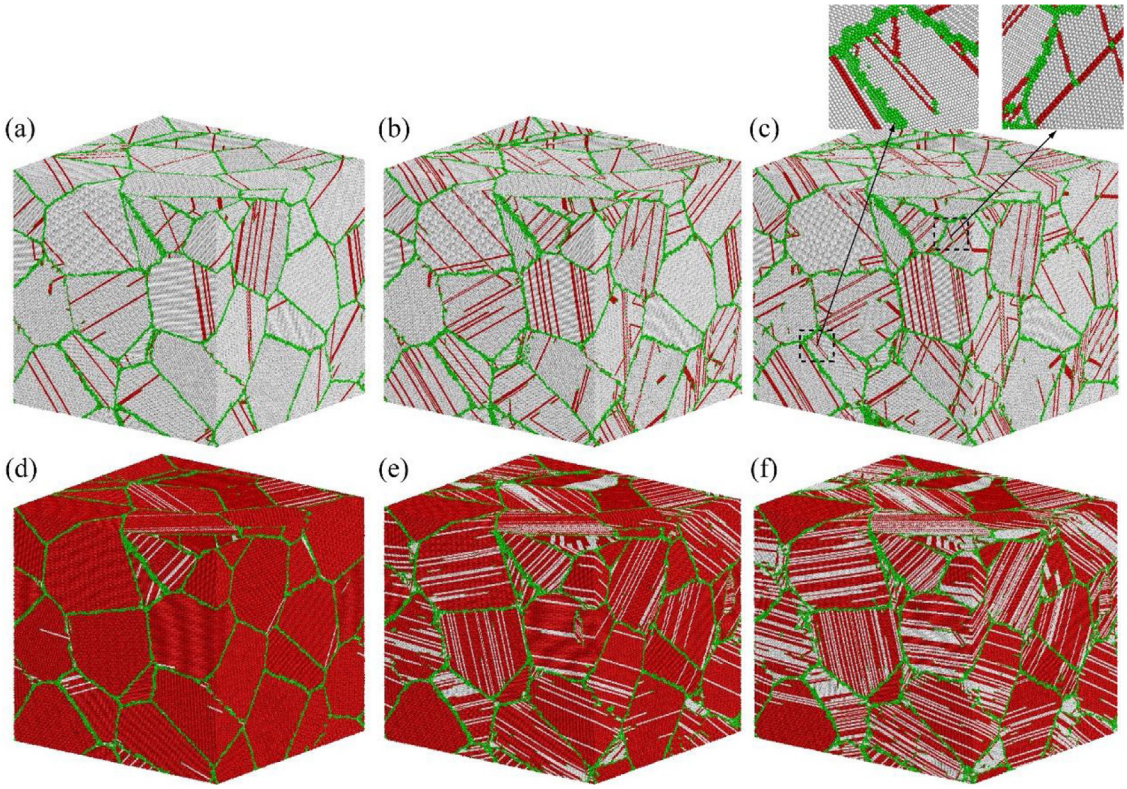

Fig. 6. Snapshots for the pure fcc sample at various applied tensile strains: (a) 4 %; (b) 7 %: (c) 10 %. Snapshots for the pure hcp sample at various applied tensile strains: (d) 4 %; (e) 7 %: (f) 10 %.

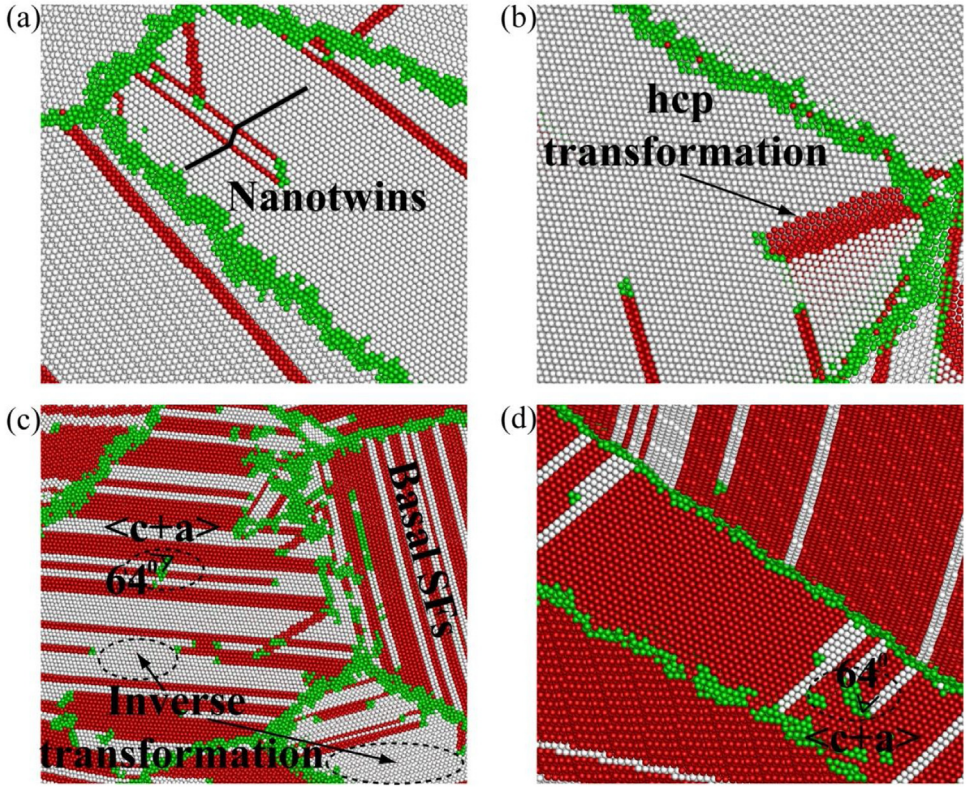

Fig. 7. The detailed atomistic deformation mechanisms for the pure fcc sample at applied tensile strains of 10 % showing (a) deformation-induced nanotwins; (b) hcp phase transformation; (c, d) The detailed atomistic deformation mechanisms for the pure hcp sample at applied tensile strains of 10 % showing basal SFs, reverse transformation (from hcp phase to fcc phase) and < c + a > edge dislocations ($1/6[2\bar{2}03]$).

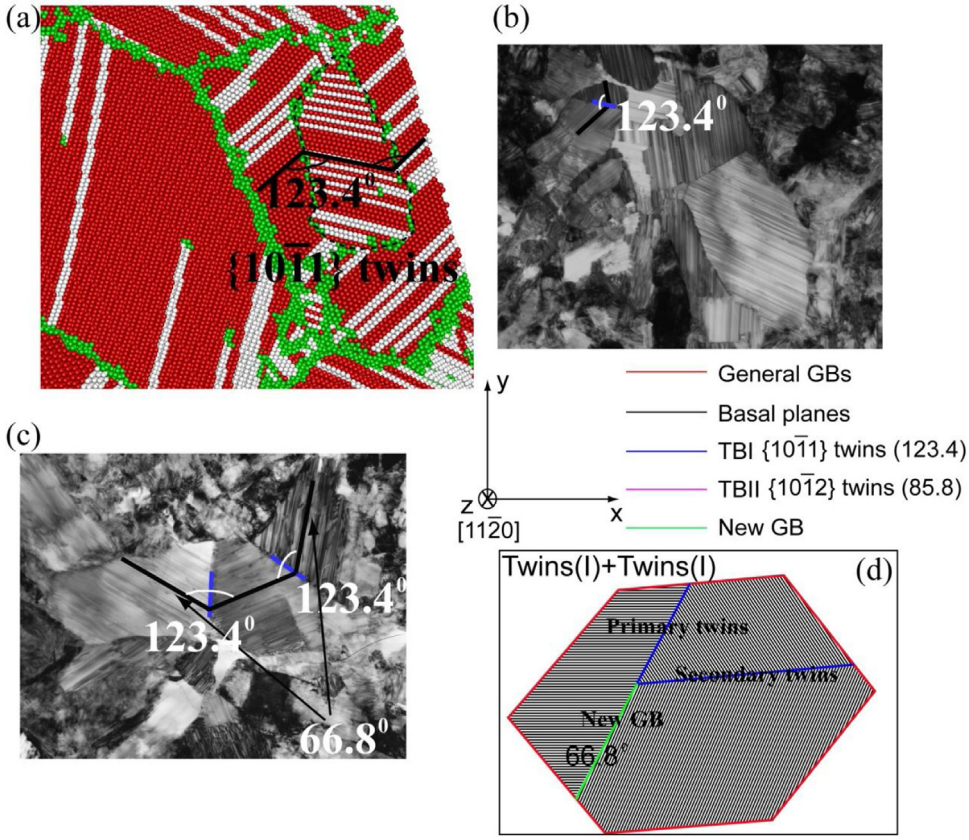

Fig. 8. (a) The detailed atomistic deformation mechanisms for the pure hcp sample at applied tensile strains of 10 % showing {10$\bar{1}$1} twins. Experimental TEM observations for the DTs in the hcp cobalt sample after SMAT: (b) The {10$\bar{1}$1} twins; (c) The secondary {10$\bar{1}$1} twins generated inside the primary {10$\bar{1}$1} twins. (d) Schematic of formation sequences and orientations of the secondary {10$\bar{1}$1} twins inside the primary {10$\bar{1}$1} twins.

shown in Fig. 5(a), and is plotted in Fig. 5(b). As indicated in the previous research [31], the flow stress was observed to increase with increasing amount of the hcp phase (ε martensite) in a Co-27Cr-5Mo-0.05C alloy, and the hcp phase (ε martensite) was found to be stronger than the fcc matrix. Our simulation results also show that the pure hcp phase has a higher average flow stress than the pure fcc phase, as indicated in Fig. 5(b).

In order to understand why the pure hcp sample is stronger than the pure fcc sample, the detailed atomistic deformation mechanisms for these two samples are revealed. The snapshots at various applied tensile strains (4 %, 7 %, and 10 %) for these two samples are displayed in Fig. 6. In the pure fcc sample, nanotwins are formed and hcp transformation (as indicated in the close-up views in Fig. 7(a) and (b)) is observed during the tensile deformation. Moreover, interactions between partial dislocations and SFs at two different slip systems, interactions between partial dislocations and TBs are also observed during the tensile deformation for the pure fcc sample (as indicated in the insets of Fig. 6(c)). As indicated in Figs. 6(d)-(f) and 7 (c), reverse phase transformation from hcp phase to fcc phase occurs during the tensile deformation for the pure hcp sample, and the fraction of fcc phase increases with increasing tensile strains.

This reverse phase transformation is achieved by the glide of basal edge dislocations on every other basal planes simultaneously or one by one, leaving basal SFs behind for the formation of fcc phase. Thus, the mechanism behind the reverse phase transformation is due to the glide of basal edge dislocations and the formation of basal SFs at adjacent planes, which only requires low critical resolved shear stress [61]. The basal edge dislocation has a Burgers vector of 2/3[1$\bar{1}$00], and these formed basal SFs are mostly identified as I_2 type intrinsic SFs, according to our previous research [61].

The formations of basal SFs and new fcc phase themselves in hcp metals should contribute little to the strengthening due to the easy slip and low critical resolved shear stress for basal planes, while the interactions of basal SFs and formed new straight phase boundaries with other dislocations might contribute to the strengthening [61,62]. These other dislocations could be < c + a > dislocations, as indicated in Fig. 7(c) and (d). Much higher critical resolved shear stress is required for nucleation of < c + a > dislocations due to their large Burges vector, which is identified as 1/6[2$\bar{2}$03] and the dislocation line has an angle of 64° with the basal planes according to our previous research [62]. These < c + a > dislocations should contribute significantly to the enhanced strain hardening

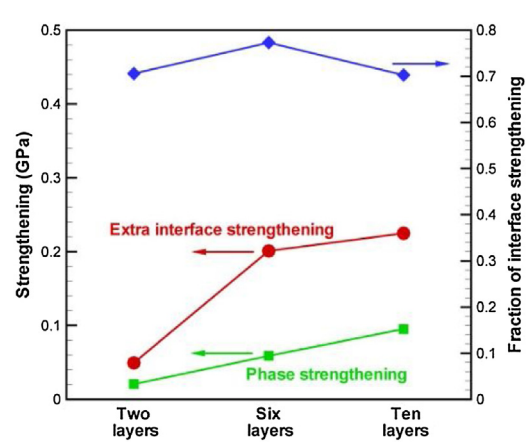

Fig. 9. The effect of hcp layer width on the strengthening.

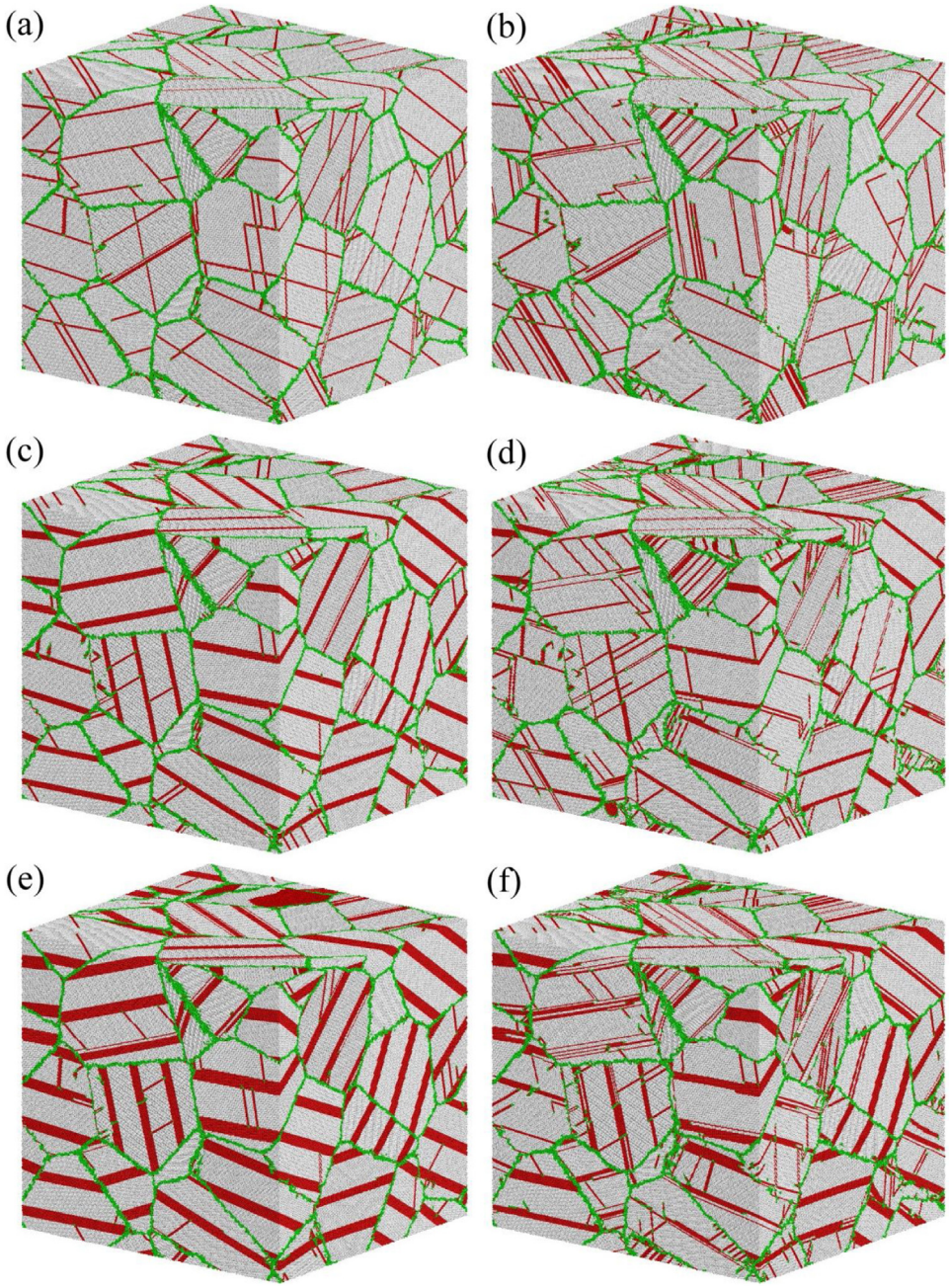

Fig. 10. Snapshots at applied tensile strains of 4 % (a, c, e) and 7 % (b, d, f) for the nanocrystalline samples (a, b) with numerous embedded SFs; (c, d) with numerous embedded six hcp atom layers; (e, f) with numerous embedded ten hcp atom layers. The interspacing is kept the same (7.34 nm) for these three samples.

and strengthening during tensile deformation in hcp metals due to their difficult nucleation and glide [62,63].

Besides the aforementioned deformation mechanisms, nucleation and growth of $\{10\bar{1}1\}$ twins are also observed during tensile deformation for the pure hcp sample, as indicated in Fig. 8(a). The newly formed TBs for $\{10\bar{1}1\}$ twins are not straight and incoherent, which are observed to deviate from $\{10\bar{1}1\}$ twinning planes. However, the misorientation angle between the newly formed $\{10\bar{1}1\}$ twins and the matrix is still close to the theoretical value of 123.4° [64]. This non-classical twinning behavior has also been observed by TEM after dynamic deformation in cobalt [64], and the corresponding formation mechanism was proposed to be a homogeneous shear plus atomic shuffling. The formation of $\{10\bar{1}1\}$ twins has been indicated to play import roles on the strain hardening and strengthening in hcp metals [65,66]. For example, the $\{10\bar{1}1\}$ twins and the secondary $\{10\bar{1}1\}$ twins generated inside the primary $\{10\bar{1}1\}$ twins have been found to be formed in the surface layer of the hcp cobalt sample after surface mechanical attrition treatment (SMAT), as indicated in Fig. 8(b) and (c). The schematic of formation sequences and orientations of the multiple twins is displayed in Fig. 8(d). The detailed experimental procedure for producing these twins in the hcp cobalt sample can be found in our previous papers [62,65]. The hardness/strength of the surface layer is much higher compared to that for the untreated sample, which can be attributed to the formation of these twins [62,65]. Thus, the higher flow stress in the pure hcp sample compared to that for the pure fcc sample, can be attributed to the aforementioned deformation mechanisms, such as the interactions of basal SFs and formed new straight phase boundaries with $1/6[2\bar{2}03]$ <c + a > dislocations, and the formation of twins.

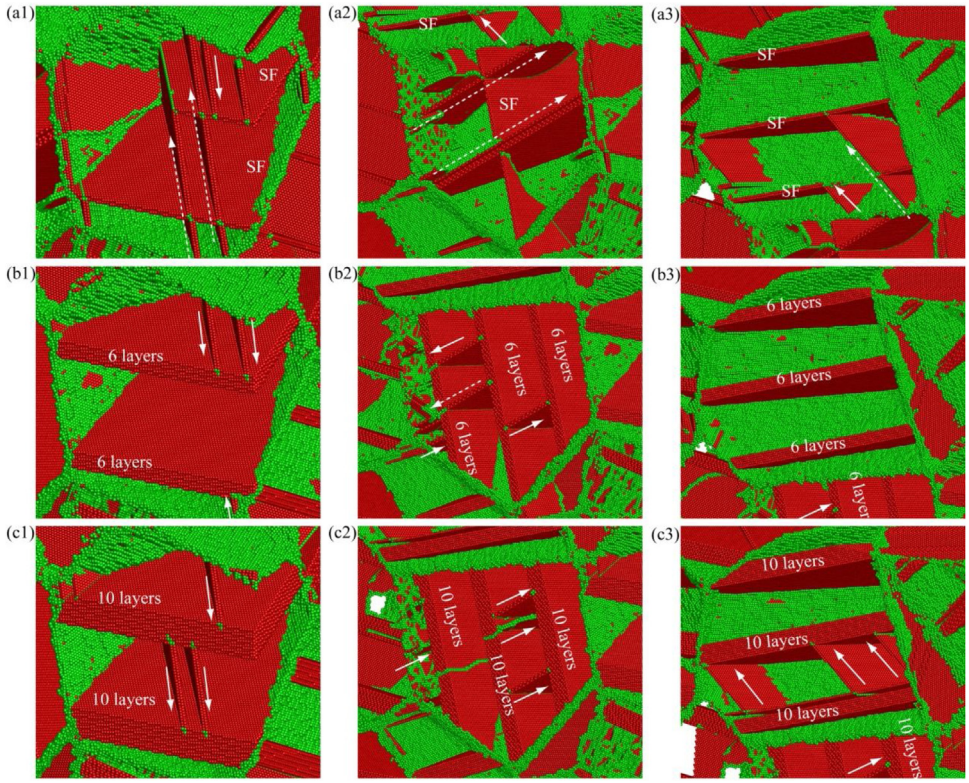

Fig. 11. The detailed atomistic deformation mechanisms for the nanocrystalline samples (a1-a3) with numerous embedded SFs; (b1-b3) with numerous embedded six hcp atom layers; (c1-c3) with numerous embedded ten hcp atom layers at the applied tensile strain of 4 %. The fcc atoms are not shown in this figure for the more clarity.

Without considering the extra interface strengthening, the average flow stress for two-phase materials can be estimated by the rule of mixture (ROM) as following:

$$\overline{\sigma}_{ROM} = \overline{\sigma}_{fcc} f_{fcc} + \overline{\sigma}_{hcp} f_{hcp} \quad (1)$$

where $\overline{\sigma}_{fcc}, \overline{\sigma}_{hcp}$ are the average flow stresses for the pure fcc sample and the pure hcp sample, respectively. f_{fcc}, f_{hcp} are the volume fractions of the fcc phase and hcp phase in the dual-phase materials, respectively.

The overall strengthening of various samples over the pure fcc sample can be calculated as:

$$\Delta\sigma_{overall} = \overline{\sigma} - \overline{\sigma}_{fcc} \quad (2)$$

where $\overline{\sigma}$ is the average flow stress for various samples.

Moreover, the phase strengthening can be calculated as:

$$\Delta\sigma_{phase} = \overline{\sigma}_{ROM} - \overline{\sigma}_{fcc} \quad (3)$$

The deformation-induced hcp phase generally has a lamellar structure, and the straight phase boundaries should be barriers for further dislocation glide since either < c> or < c + a > dislocations are required for the transmission of the edge dislocations into hcp nano-lamellae and very high critical resolved shear stress is typically required for activation of these types of dislocations [28]. Thus, besides the phase strengthening, the extra interface strengthening should be considered and can be calculated as the following equation:

$$\Delta\sigma_{interface} = \overline{\sigma} - \overline{\sigma}_{ROM} \quad (4)$$

In this regard, the overall strengthening should have two components: the phase strengthening and the extra interface strengthening. And, the fraction of the extra interface strengthening in the overall strengthening can be calculated as following:

$$f_{interfacestrengthening} = \Delta\sigma_{interface} / \Delta\sigma_{overall} \quad (5)$$

The phase strengthening, the extra interface strengthening and the fraction of interface strengthening are plotted as a function of the width of nano-lamellae in Fig. 9. It is interesting to note that both the phase strengthening and the extra interface strengthening increase with increasing width of hcp nano-lamellae when the interspacing is fixed. With increasing width of hcp nano-lamellae, the rising trend for the phase strengthening is straightforward due to the increasing volume fraction of the harder hcp phase. While, the extra interface strengthening (over 70 % of overall strengthening) is found to be much stronger than the phase strengthening, and also is observed to increase with increasing width of nano-lamellae. The corresponding atomistic deformation mechanisms will be provided next.

The snapshots at various applied tensile strains (4 % and 7 %) for the nanocrystalline samples with different widths of hcp nano-lamellae (embedded SFs; embedded six hcp atom layers and embedded ten hcp atom layers) are displayed in Fig. 10, in these samples the interspacing is kept the same (7.34 nm) to investigate the effect of the width of hcp nano-lamellae. The close-up views for Fig. 10 showing the interactions between partial dislocations and phase boundaries are displayed in Fig. 11. In Fig. 11, the original embedded two hcp layers (SFs), six hcp atom layers and ten hcp atom layers are marked, and the moving partial dislocations interacting with these hcp nano-lamellae are also indicated by solid or dash lines with arrows. The solid lines with arrows indicate that the partial dislocations are blocked by the embedded SFs/hcp lamellae, while the dash lines with arrows represent that the partial dislocations cut through the embedded SFs/hcp lamellae. It has been reported that SFs can significantly strengthen the nanowires/nanorods by restricting dislocation activities between nanoscale neighboring SFs [67]. The strengthening by basal SFs has also been reported in Mg alloys [68–70], and the strengthening effect was found to increase linearly with the reciprocal of the SF interspacing due to the interactions between the basal SFs and

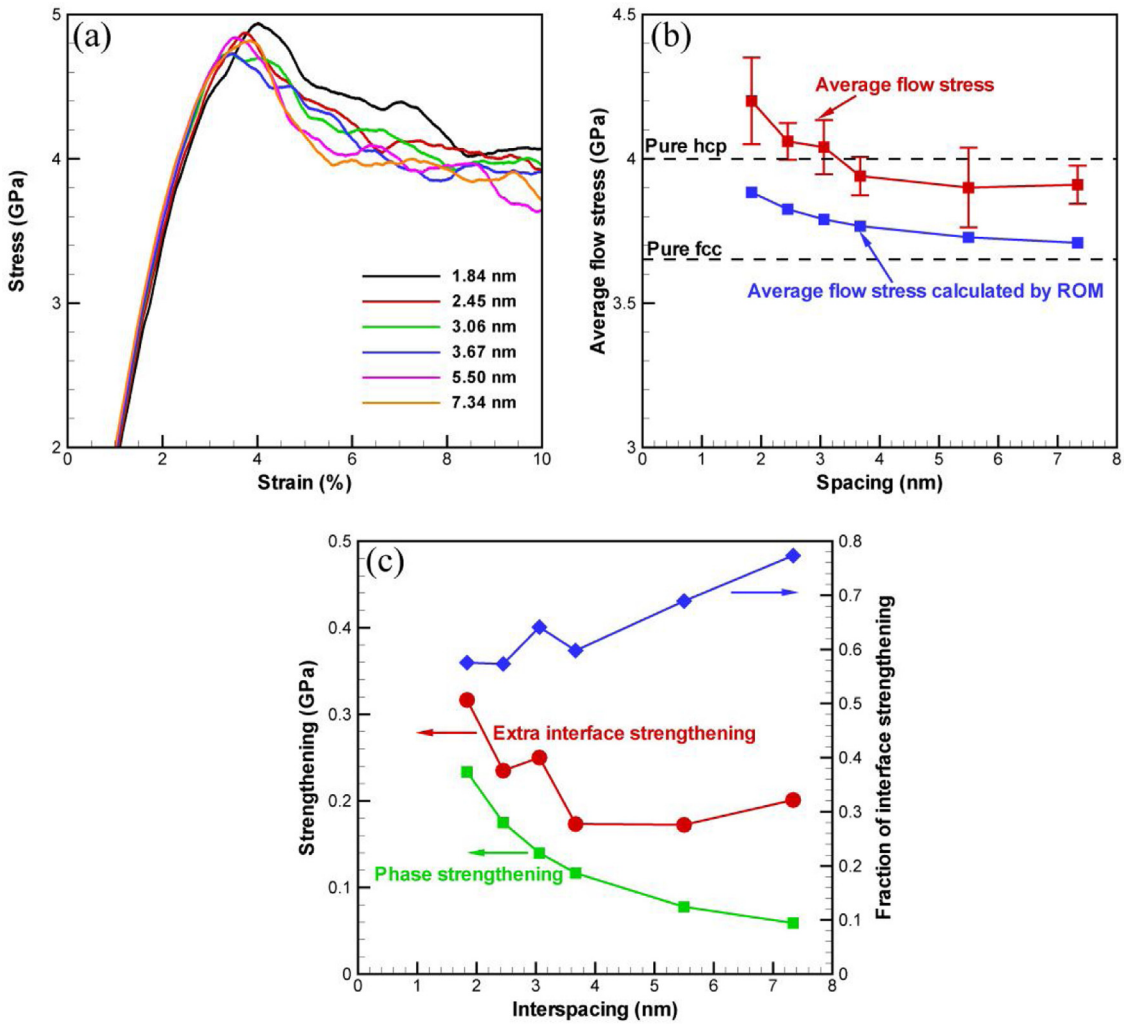

Fig. 12. (a) The simulated stress-strain curves for the 3D nanocrystalline samples with the same hcp layer width (six hcp atom layers) and the different interspacings. (b) The effect of interspacing on the average flow stress. (c) The effect of interspacing on the strengthening.

the < c + a > dislocations. As we know, SFs are the thinnest hcp nano-lamellae (two atomic hcp layers), and the SFs were found to have strengthening effect indeed in polycrystalline fcc materials, as shown in Figs. 5 and 9. However, this strengthening effect becomes more remarkable when the width of hcp nano-lamellae is larger (Fig. 5(b)). Excluding the phase strengthening effect, the extra interface strengthening was also found to increase with increasing width of hcp nano-lamellae (Fig. 9). As indicated in Figs. 10(a) and 11 (a1)-(a3), the partial dislocations can cut through most embedded SFs, only a few dislocations are observed to be blocked by them at the applied tensile strain of 4 %. While, most partial dislocations are blocked by the embedded six hcp layers (Figs. 10(c) and 11 (b1)-(b3)), and all partial dislocations are blocked by the embedded ten hcp layers (Figs. 10(e) and 11 (c1)-(c3)). These observations indicate that the embedded SFs/hcp nano-lamellae are barriers for dislocation glide and the blocking ability becomes stronger as the width of hcp nano-lamellae increases, resulting in larger extra interface strengthening effect for the samples with larger width of hcp nano-lamellae. It has been indicated that hetero-deformation-induced (HDI) strengthening should play an important role in the materials with different phases due to the difference in strength for different phases [71], which is the extra strengthening beyond ROM. The HDI strengthening is originated from the formation of geometrically necessary dislocations at the interfaces, which is similar to the interface strengthening mentioned in the present study.

3.3. *Effect of interspacing of hcp nano-lamellae on the strengthening*

Second, the effect of the interspacing of hcp nano-lamellae on the tensile properties is investigated by MD simulations as the width of hcp nano-lamellae is fixed as six hcp atom layers. Fig. 12(a) displays the simulated stress-strain curves for the nanocrystalline samples with different interspacings (1.84, 2.48, 3.06, 3.67, 5.50, 7.34 nm) while with the same width of hcp nano-lamellae. Again, the average stress over a strain interval from 6 % to 10% is calculated for various samples shown in Fig. 12(a), and is plotted as a function of interspacing in Fig. 12(b). Moreover, the average flow stress calculated by ROM (only considering the phase strengthening by Eq. (1)) is also plotted as a function of interspacing in Fig. 12(b). The average flow stresses for the pure fcc sample and the pure hcp sample are also included in Fig. 12(b) as dash lines for comparison. It is interesting to note that the average flow stresses for the three samples with smaller interspacings (1.84, 2.45, 3.06 nm) are even higher than that for the sample with pure hard hcp phase, due to the extra interface strengthening. The phase strengthening, the extra interface strengthening and the fraction of interface strengthening are plotted as a function of interspacing in Fig. 12(c). It is observed that both the phase strengthening and the extra interface strengthening increase with decreasing interspacing when the width of hcp nano-lamellae is fixed. The rising trend for the phase strengthen-

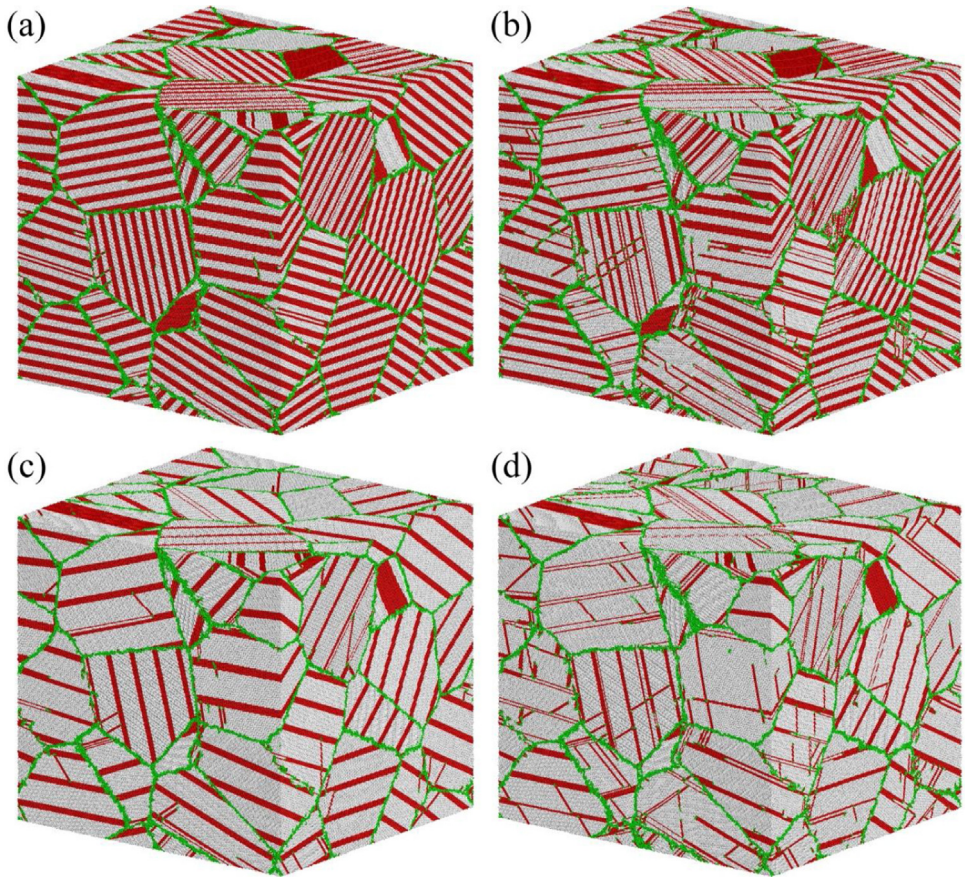

Fig. 13. Snapshots at applied tensile strains of 4 % (a, c) and 7 % (b, d) for the nanocrystalline samples: (a-b) The interspacing is 2.45 nm; (b) The interspacing is 5.50 nm. The width of hcp nano-lamellae is fixed (six hcp atom layers) for these two samples.

ing with decreasing interspacing can be easily understood since the volume fraction of hcp phase becomes larger with decreasing interspacing. While, the extra interface strengthening is always stronger than the phase strengthening for all samples, and the fraction of the interface strengthening is always over 50 % of overall strengthening although the fraction of the interface strengthening decreases with decreasing interspacing.

The snapshots at various applied tensile strains (4 % and 7 %) for the nanocrystalline samples with different interspacings (2.48 and 5.50 nm) are displayed in Fig. 13, in these two samples the width of the hcp nano-lamellae is kept the same (embedded six hcp atom layers) to investigate the effect of interspacing on the deformation mechanisms. The close-up views for Fig. 13 showing the details for the atomistic deformation mechanisms are displayed in Fig. 14. Two dominant deformation mechanisms are observed for these samples: (i) the interactions between partial dislocations and phase boundaries (Fig. 14(a1)-(a2) and (b1)-(b2)); (ii) the nucleation and glide of partial dislocations along/parallel to the phase boundaries, some of them inducing reverse phase transformation (from hcp phase to fcc phase) or DTs (formation of nanotwins in hcp nano-lamellae, as shown in Fig. 14(a3) and (b3)). It has been reported that the strength of nanotwinned fcc metals first increases as twin boundary spacing (TBS) decreases, reaching a maximum at a critical TBS, and then decreases as TBS becomes even smaller [56]. The softening with decreasing TBS below the critical TBS in the nanotwinned fcc metals has been attributed to a transition of the dominant deformation mechanism from the classical Hall-Petch type strengthening above the critical TBS due to the interaction between dislocations and TBs to a dislocation-nucleation-controlled softening mechanism below the critical TBS with TB migration [56]. In the nanocrystalline fcc samples with embedded hcp nano-lamellae for the present study, it seems that there is no such a transition for the dominant deformation mechanism. No matter the spacing is larger or small, both mechanisms, i.e. the interaction between partial dislocations from other slip systems with phase boundaries and the nucleation/glide of partial dislocations along/parallel to the phase boundaries, are important and can't be ignored. Moreover, the formed TBs (Fig. 14(a3) and (b3)) can also be strong barriers for dislocation slip even when the partial dislocations glide along/parallel to the phase boundaries, resulting in strong strengthening [16,56]. As indicated, the density of the phase boundaries and the newly formed TBs is higher when the interspacing is smaller, thus providing more barriers for dislocation glide in the other slip systems and resulting in stronger resistance for further dislocation slip and higher strength.

4. Concluding remarks

In the present study, dynamic shear testing has been conducted on the CoCrNi MEA under both cryogenic and room temperatures, and the deformation-induced hcp nano-lamellae with various widths and interspacings were observed to be formed under cryogenic temperature. Microhardness in the cryogenic-deformed samples has been compared with the room temperature-deformed samples without hcp phase. Moreover, a series of large-scale MD simulations have been performed to reveal the effects of the width and interspacing of embedded hcp nano-lamellae on the tensile plastic flow behaviors and the corresponding atomistic deformation mechanisms in the fcc CoCrNi MEA. The main findings can be summarized as follows:

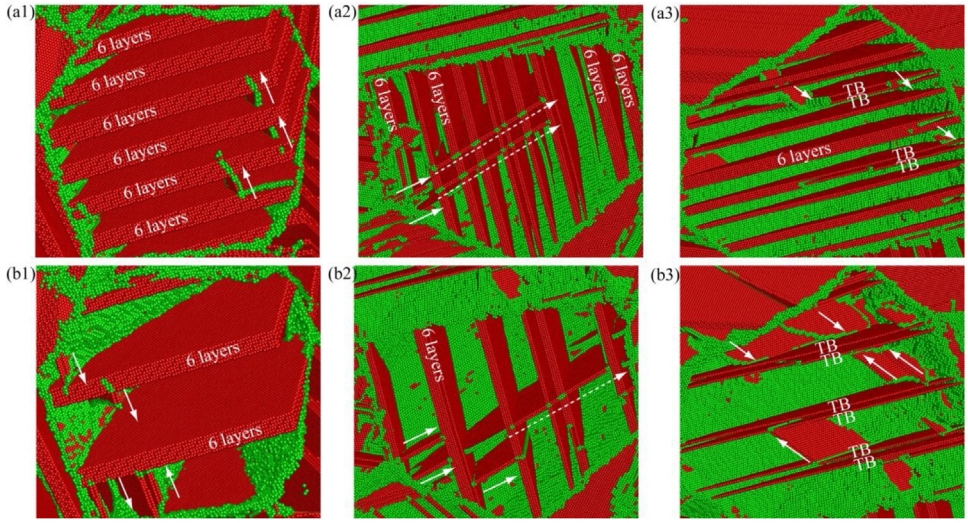

Fig. 14. The detailed atomistic deformation mechanisms for the nanocrystalline samples: (a1-a3) The interspacing is 2.45 nm; (b1-b3) The interspacing is 5.50 nm. (a1)(b1) are snapshots at the applied tensile strain of 4 %; while (a2)(a3)(b2)(b3) are snapshots at the applied tensile strain of 7 %. The fcc atoms are not shown in this figure for the more clarity.

(1) The microhardness increment after dynamic shear deformation under cryogenic temperature (0.69 GPa) is much higher than that after dynamic shear deformation under room temperature (0.42 GPa). This observation qualitatively shows the experimental evidence that deformation-induced hcp nano-lamellae can have strong effect on the strengthening.
(2) The pure hcp phase (ε martensite) was found to be stronger than the pure fcc phase in the CoCrNi MEA, due to the formations of the < c + a > dislocations and the $\{10\bar{1}1\}$ twins. Thus, the overall strengthening in the nanocrystalline fcc CoCrNi MEA samples with embedded hcp nano-lamellae was found to have two components: the phase strengthening and the extra interface strengthening. The extra interface strengthening was observed to be always stronger than the phase strengthening.
(3) Both the overall strengthening and the interface strengthening were observed to increase as the width of embedded hcp nano-lamellae increases. The embedded hcp nano-lamellae are barriers for dislocation glide in the other slip systems, and the blocking ability becomes stronger as the width of hcp nano-lamellae increases, resulting in larger extra interface strengthening effect.
(4) Both the overall strengthening and the interface strengthening were also found to increase with decreasing interspacing of embedded hcp nano-lamellae. The samples with small interspaced hcp nano-lamellae are even stronger than the pure hard hcp phase due to the extra interface strengthening. No matter the interspacing is larger or small, both deformation mechanisms are important and can't be ignored: (i) the interactions between partial dislocations and phase boundaries; (ii) the nucleation and glide of partial dislocations along/parallel to the phase boundaries, some of them inducing reverse phase transformation or formation of nanotwins in hcp nano-lamellae. The density of the phase boundaries and the newly formed TBs is higher when the interspacing is smaller, thus providing more barriers for dislocation glide in the other slip systems and resulting in higher strength. These results should provide insights for tailoring microstructures to achieve better mechanical properties.

Declaration of Competing Interest

The authors declare that they have no known competing financial interests or personal relationships that could have appeared to influence the work reported in this paper.

Acknowledgements

This work was supported by the National Key R&D Program of China [grant numbers 2017YFB0202802, 2017YFA0204402 and 2019YFA02099-01/-02], the NSFC Basic Science Center Program for "Multiscale Problems in Nonlinear Mechanics" [grant number 11988102], the National Natural Science Foundation of China [grant numbers 11672313, 11790293 and 52071326], and the Strategic Priority Research Program of the Chinese Academy of Sciences [grant number XDB22040503].

References

[1] J.W. Yeh, S.K. Chen, S.J. Lin, J.Y. Gan, T.S. Chin, T.T. Shun, C.H. Tsau, S.Y. Chang, Adv. Eng. Mater. 6 (2004) 299–303.
[2] Y.H. Jo, S. Jung, W.M. Choi, S.S. Sohn, H.S. Kim, B.J. Lee, N.J. Kim, S. Lee,Nat. Commun. 8 (2017), 15719.
[3] E.P. George, D. Raabe, R.O. Ritchie, Nat. Rev. Mater. 4 (2019) 515–534.
[4] M. Yang, D. Yan, F. Yuan, P. Jiang, E. Ma, X. Wu, Proc. Natl. Acad. Sci. U. S. A. 115 (2018) 7224–7229.
[5] B. Gludovatz, A. Hohenwarter, K.V.S. Thurston, H. Bei, Z. Wu, E.P. George, R.O. Ritchie,Nat. Commun. 7 (2016), 10602.
[6] B. Gan, J.M. Wheeler, Z.N. Bi, L. Liu, J. Zhang, H.Z. Fu, J. Mater. Sci. Technol. 35 (2019) 957–961.
[7] Z. Lei, X. Liu, Y. Wu, H. Wang, S. Jiang, S. Wang, X. Hui, Y. Wu, B. Gault, P. Kontis, D. Raabe, L. Gu, Q. Zhang, H. Chen, H. Wang, J. Liu, K. An, Q. Zeng, T.-G. Nieh, Z. Lu, Nature 563 (2018) 546–550.
[8] Z. Zhang, H. Sheng, Z. Wang, B. Gludovatz, Z. Zhang, E.P. George, Q. Yu, S.X. Mao, R.O. Ritchie, Nat. Commun. 8 (2017) 14390.
[9] B. Cantor, I.T.H. Chang, P. Knight, A.J.B. Vincent, Mater. Sci. Eng. A 375 (2004) 213–218.
[10] B. Gludovatz, A. Hohenwarter, D. Catoor, E.H. Chang, E.P. George, R.O. Ritchie, Science 345 (2014) 1153–1158.
[11] B. Schuh, F. Mendez-Martin, B. Voelker, E.P. George, H. Clemens, R. Pippan, A. Hohenwarter, Acta Mater. 96 (2015) 258–268.
[12] L.X. Yang, H.L. Ge, J. Zhang, T. Xiong, Q.Q. Jin, Y.T. Zhou, X.H. Shao, B. Zhang, Z.W. Zhu, S.J. Zheng, X.L. Ma, J. Mater. Sci. Technol. 35 (2019) 300–305.

[13] M. Yang, L. Zhou, C. Wang, P. Jiang, F. Yuan, E. Ma, X. Wu, Scr. Mater. 172 (2019) 66–71.
[14] X. Wu, M. Yang, P. Jiang, C. Wang, L. Zhou, F. Yuan, E. Ma, Scr. Mater. 178 (2020) 452–456.
[15] P. Shi, W. Ren, T. Zheng, Z. Ren, X. Hou, J. Peng, P. Hu, Y. Gao, Y. Zhong, P.K. Liaw, Nat. Commun. 10 (2019) 489.
[16] Z. Yang, M. Yang, Y. Ma, L. Zhou, W. Cheng, F. Yuan, X. Wu,Mater. Sci. Eng. A 793 (2020), 139854.
[17] Y. Han, H. Li, H. Feng, K. Li, Y. Tian, Z. Jiang, J. Mater. Sci. Technol. 65 (2021) 210–215.
[18] J. Li, L. Li, C. Jiang, Q.H. Fang, F. Liu, Y. Liu, P.K. Liaw, J. Mater. Sci. Technol. 57 (2020) 85–91.
[19] F.X. Zhang, S. Zhao, K. Jin, H. Xue, G. Velisa, H. Bei, R. Huang, J.Y.P. Ko, D.C. Pagan, J.C. Neuefeind, W.J. Weber, Y. Zhang,Phys. Rev. Lett. 118 (20) (2017), 205501.
[20] Q.J. Li, H. Sheng, E. Ma, Nat. Commun. 10 (2019) 3563.
[21] R. Zhang, S. Zhao, J. Ding, Y. Chong, T. Jia, C. Ophus, M. Asta, R.O. Ritchie, A.M. Minor, Nature 581 (2020) 283–287.
[22] F. Zhang, Y. Tong, K. Jin, H. Bei, W.J. Weber, A. Huq, A. Lanzirotti, M. Newville, D.C. Pagan, J.Y.P. Ko, Y. Zhang, Mater. Res. Lett. 6 (2018) 450–455.
[23] J. Ding, Q. Yu, M. Asta, R.O. Ritchie, Proc. Natl. Acad. Sci. U. S. A. 115 (2018) 8919–8924.
[24] Q. Ding, Y. Zhang, X. Chen, X. Fu, D. Chen, S. Chen, L. Gu, F. Wei, H. Bei, Y. Gao, M. Wen, J. Li, Z. Zhang, T. Zhu, R.O. Ritchie, Q. Yu, Nature 574 (2019) 223–227.
[25] S.S. Sohn, A.K. da Silva, Y. Ikeda, F. Koermann, W. Lu, W.S. Choi, B. Gault, D. Ponge, J. Neugebauer, D. Raabe,Adv. Mater. 31 (2019), 1807142.
[26] H. Luo, S.S. Sohn, W. Lu, L. Li, X. Li, C.K. Soundararajan, W. Krieger, Z. Li, D. Raabe, Nat. Commun. 11 (2020) 3081.
[27] C. Niu, C.R. LaRosa, J. Miao, M.J. Mills, M. Ghazisaeidi, Nat. Commun. 9 (2018) 1363.
[28] Y. Ma, F. Yuan, M. Yang, P. Jiang, E. Ma, X. Wu, Acta Mater. 148 (2018) 407–418.
[29] W. Wu, L. Guo, B. Guo, Y. Liu, M. Song, Mater. Sci. Eng. A 759 (2019) 574–582.
[30] Q. Lin, J. Liu, X. An, H. Wang, Y. Zhang, X. Liao, Mater. Res. Lett. 6 (2018) 236–243.
[31] A. Mani, R. Salinas, H.F. Lopez, Mater. Sci. Eng. A 528 (2011) 3037–3043.
[32] I. Weissensteiner, M. Petersmann, P. Erdely, A. Stark, T. Antretter, H. Clemens, V. Maier-Kiener, Acta Mater. 164 (2019) 272–282.
[33] J.W. Bae, J.B. Seol, J. Moon, S.S. Sohn, M.J. Jang, H.Y. Um, B.-J. Lee, H.S. Kim, Acta Mater. 161 (2018) 388–399.
[34] Z. Li, K.G. Pradeep, Y. Deng, D. Raabe, C.C. Tasan, Nature 534 (2016) 227, -+.
[35] P. Yu, R. Feng, J. Du, S. Shinzato, J.-P. Chou, B. Chen, Y.-C. Lo, P.K. Liaw, S. Ogata, A. Hu, Acta Mater. 181 (2019) 491–500.
[36] S. Chen, H.S. Oh, B. Gludovatz, S.J. Kim, E.S. Park, Z. Zhang, R.O. Ritchie, Q. Yu, Nat. Commun. 11 (2020) 826.
[37] C.E. Slone, J. Miao, E.P. George, M.J. Mills, Acta Mater. 165 (2019) 496–507.
[38] W. Guo, Z. Pei, X. Sang, J.D. Poplawsky, S. Bruschi, J. Qu, D. Raabe, H. Bei, Acta Mater. 170 (2019) 176–186.
[39] J. Miao, C.E. Slone, T.M. Smith, C. Niu, H. Bei, M. Ghazisaeidi, G.M. Pharr, M.J. Mills, Acta Mater. 132 (2017) 35–48.
[40] X.L. Ma, C.X. Huang, W.Z. Xu, H. Zhou, X.L. Wu, Y.T. Zhu, Scr. Mater. 103 (2015) 57–60.
[41] X. Ma, C. Huang, J. Moering, M. Ruppert, H.W. Hoeppel, M. Goeken, J. Narayan, Y. Zhu, Acta Mater. 116 (2016) 43–52.
[42] C.X. Huang, Y.F. Wang, X.L. Ma, S. Yin, H.W. Hoeppel, M. Goeken, X.L. Wu, H.J. Gao, Y.T. Zhu, Mater. Today 21 (2018) 713–719.
[43] C. Zhao, J. Li, Y. Liu, W.Y. Wang, H. Kou, E. Beaugnon, J. Wang, J. Mater. Sci. Technol. 73 (2021) 83–90.
[44] I.J. Beyerlein, J.R. Mayeur, S. Zheng, N.A. Mara, J. Wang, A. Misra, Proc. Natl. Acad. Sci. U. S. A. 111 (2014) 4386–4390.
[45] R. Yuan, I.J. Beyerlein, C. Zhou, Mater. Res. Lett. 5 (2017) 251–257.
[46] J. He, Y. Ma, D. Yan, S. Jiao, F. Yuan, X. Wu, Mater. Sci. Eng. A 726 (2018) 288–297.
[47] J. He, F. Yuan, M. Yang, S. Jiao, X. Wu, Mater. Sci. Eng. A 756 (2019) 492–501.
[48] J. He, F. Yuan, M. Yang, L. Zhou, S. Jiao, X. Wu,Mater. Sci. Eng. A 791 (2020), 139780.
[49] S.I. Rao, C. Varvenne, C. Woodward, T.A. Parthasarathy, D. Miracle, O.N. Senkov, W.A. Curtin, Acta Mater. 125 (2017) 311–320.
[50] E. Antillon, C. Woodward, S.I. Rao, B. Akdim, T.A. Parthasarathy, Acta Mater. 166 (2019) 658–676.
[51] J. Li, H.T. Chen, H. Feng, Q.H. Fang, Y. Liu, F. Liu, H. Wu, P.K. Liaw, J. Mater. Sci. Technol. 54 (2020) 14–19.
[52] J. Li, B. Xie, Q. Fang, B. Liu, Y. Liu, P.K. Liaw, J. Mater. Sci. Technol. 68 (2021) 70–75.
[53] S.I. Rao, C. Woodward, T.A. Parthasarathy, O. Senkov, Acta Mater. 134 (2017) 188–194.
[54] V. Yamakov, D. Wolf, S.R. Phillpot, A.K. Mukherjee, H. Gleiter, Nat. Mater. 1 (2002) 45–48.
[55] J. Schiotz, K.W. Jacobsen, Science 301 (2003) 1357–1359.
[56] X. Li, Y. Wei, L. Lu, K. Lu, H. Gao, Nature 464 (2010) 877–880.
[57] D. Farkas, A. Caro, J. Mater. Res. 33 (2018) 3218–3225.
[58] F. Yuan, W. Cheng, S. Zhang, X. Liu, X. Wu,Materialia 9 (2020), 100565.
[59] O. Grassel, L. Kruger, G. Frommeyer, L.W. Meyer, Int. J. Plast. 16 (2000) 1391–1409.
[60] A. Misra, J.P. Hirth, R.G. Hoagland, Acta Mater. 53 (2005) 4817–4824.
[61] W. Wang, P. Jiang, F. Yuan, X. Wu, Philos. Mag. 98 (2018) 1186–1203.
[62] W. Wang, F. Yuan, P. Jiang, X. Wu, Sci. Rep. 7 (2017) 9550.
[63] B. Li, P.F. Yan, M.L. Sui, E. Ma, Acta Mater. 58 (2010) 173–179.
[64] X.Y. Zhang, B. Li, J. Tu, Q. Sun, Q. Liu, Mater. Res. Lett. 3 (2015) 142–148.
[65] X. Wu, N. Tao, Y. Hong, G. Liu, B. Xu, J. Lu, K. Lu, Acta Mater. 53 (2005) 681–691.
[66] B. Li, E. Ma, Acta Mater. 57 (2009) 1734–1743.
[67] J. Wang, Y.G. Shen, F. Song, F.J. Ke, Y.L. Bai, C. Lu, EPL 110 (2015) 36002.
[68] W.W. Jian, G.M. Cheng, W.Z. Xu, C.C. Koch, Q.D. Wang, Y.T. Zhu, S.N. Mathaudhu,Appl. Phys. Lett. 103 (2013), 133108.
[69] W.W. Jian, G.M. Cheng, W.Z. Xu, H. Yuan, M.H. Tsai, Q.D. Wang, C.C. Koch, Y.T. Zhu, S.N. Mathaudhu, Mater. Res. Lett. 1 (2013) 61–66.
[70] C. Xu, J. Zhang, S. Liu, Y. Jing, Y. Jiao, L. Xu, L. Zhang, F. Jiang, M. Zhang, R. Wu, Mater. Des. 79 (2015) 53–59.
[71] Y.T. Zhu, X.L. Wu, Mater. Res. Lett. 7 (2019) 393–398.